

Experimental and quantum-chemical studies on the three-particle fragmentation of neutral triatomic hydrogen

Ulrich Galster, Frank Baumgartner, Ulrich Müller, and Hanspeter Helm

Department of Molecular and Optical Physics, Albert-Ludwigs-Universität, Hermann-Herder-Strasse 3, D-79104 Freiburg, Germany

Martin Jungen

Institute of Physical Chemistry, University of Basel, Klingelbergstrasse 80, CH-4056 Basel, Switzerland

(Received 6 July 2005; published 27 December 2005)

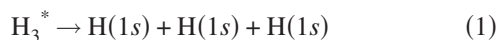
Dissociation of well-defined H_3 Rydberg states into three ground state hydrogen atoms reveals characteristic correlation patterns in the center-of-mass motion of the three fragments. We present an extensive experimental dataset of momentum correlation maps for all lower Rydberg states of H_3 and D_3 . In particular the states with principal quantum number $n=2$ feature simple correlation patterns with regular occurrence of mutual affinities. Energetically higher-lying states typically show more complex patterns which are unique for each state. Quantum-chemical calculations on adiabatic potential energy surfaces of H_3 Rydberg states are presented to illuminate the likely origin of these differences. We discuss the likely dissociation mechanisms and paths which are responsible for the observed continuum correlation.

DOI: [10.1103/PhysRevA.72.062506](https://doi.org/10.1103/PhysRevA.72.062506)

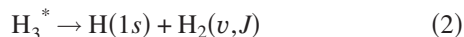
PACS number(s): 31.50.Gh, 31.25.Qm, 33.80.Gj, 34.50.Lf

I. INTRODUCTION

Dissociation and predissociation of the neutral triatomic hydrogen molecule has been a subject of intense discussion over many years. Motivated by the practical application in astrophysical processes such as dissociative recombination of H_3^+ with slow electrons [1,2] and by the challenge of understanding this prototypical system of three protons and three electrons, experiments have been refined to trace the final state distribution emerging from the predissociation of this molecule [3–6]. Electronic, vibrational, and rotational state selected Rydberg states have been investigated in this way as well as the products from dissociative recombination of slow electrons with internally cold H_3^+ ions [7]. A deeper understanding of the subtle dynamics involved in the distribution of total energy among the translational degrees of freedom in the process



and among translational and internal degrees of freedom in the competing reaction



has to date been hampered by the limited information on the potential energy surfaces and the rovibronic coupling among the excited state manifold of triatomic hydrogen.

The repulsive ground state surfaces of H_3 have been studied by theory in great detail over the past 80 years [8–13], permitting the interpretation of experimental studies of the dynamics on this potential [14–17]. Detailed information on the excited state surfaces came with the geometry-dependent quantum defect calculations by Nager and Jungen [18] and King and Morokuma [19], followed by the work of Petsalakis *et al.* [20] and Kuppermann *et al.* [21]. The quantum-chemical information from Nager and Jungen's work formed the basis for multichannel quantum defect theory (MQDT)

treatments of autoionization [22], for two-dimensional studies of the nonadiabatic coupling in reaction (2) [23] and for the recent interpretation of the high rate of dissociative recombination of slow electrons with H_3^+ invoking Jahn-Teller-type coupling [24].

The quantum-chemical information on excited states of H_3 is significantly extended in this contribution, in which highly precise surfaces over a wide range of nuclear geometries are presented. These help to discuss our experimental results on state selective predissociation of $n=2$ and $n=3$ Rydberg states of H_3 and D_3 in reaction (1). The paper is organized as follows: In Sec. II the potential energy surfaces of H_3 in hyperspherical coordinates are presented. Based on these results, we discuss the likely reaction paths suggested by open and coupled channels emerging from quantum chemistry. In Sec. III we briefly describe the experimental approach to study reaction (1) for state-selected Rydberg states. The experimental results are presented in Sec. IV, followed by a general discussion in Sec. V.

II. POTENTIAL ENERGY SURFACES

We first discuss the quantum-chemical properties of the ground and lower excited potential surfaces of the H_3 system, starting with a description of the parent ion H_3^+ . This is a continuation of our earlier studies on H_3 [18,22,25,26] as well as the work of Petsalakis *et al.* [16,20]. In part the results of a recent paper [27,63] will also be reviewed.

We use hyperspherical coordinates ρ , ϑ , φ as internal coordinates for characterizing the H_3 triangles. These coordinates are explained in detail in the Appendix. In this paper only C_{2v} arrangements are treated; in this case φ has a constant value and the hyperangle ϑ characterizes various isosceles triangles; it varies from 0° (obtuse linear) to 180° (acute linear) with 90° for the equilateral triangle. Variation of the hyperangle φ results in transforming acute isosceles

TABLE I. Energies, symmetries, and effective quantum numbers of the lower Rydberg states of H_3 for two selected geometries.

State label	Equilibrium of $H_3^+{}^a$			State label	Linear saddle point of H_3^b		
	Outer orbital ^c	E (a.u.)	n^*		Outer orbital ^{d,e}	E (a.u.)	n^*
$1^2E'$	$2pe'$	-1.55957	1.518	$1^2\Sigma_u^+$	$2p\sigma_u$	-1.65609	1.137
$1^2A'_1$	$2sa'_1$	-1.48236	1.891	$1^2\Sigma_g^+$	23%	-1.41424	1.859
$1^2A''_2$	$2pa''_2$	-1.47585	1.936	$1^2\Pi_u$	$2p\pi_u$	-1.39521	1.995
$2^2E'$	$3pe'$	-1.41623	2.604	$2^2\Sigma_g^+$	45%	-1.38566	2.075
$2^2A'_1$	$3sa'_1$	-1.40149	2.911	$2^2\Sigma_u^+$	$3p\sigma_u$	-1.35518	2.416
$2^2A''_2$	$3pa''_2$	-1.40003	2.948	$1^2\Pi_g$	$3d\pi_g$	-1.32802	2.924
$3^2E'$	$3de'$	-1.39952	2.961	$3^2\Sigma_g^+$	0%	-1.32564	2.985
$1^2E''$	$3de''$	-1.39819	2.996	$2^2\Pi_u$	$3p\pi_u$	-1.32456	3.014
$3^2A'_1$	$3da'_1$	-1.39778	3.007	$4^2\Sigma_g^+$	11%	-1.32345	3.045
				$1^2\Delta_g$	$3d\delta_g$	-1.32260	3.070
H_3^{+f}							
$1^1A'_1$		-1.34249		$1^1\Sigma_g^+$		-1.26952	

^a $\rho=2.172a_0$, $\vartheta=90^\circ$, $\varphi=0^\circ$, $r_{HH}=1.650a_0$, D_{3h} .

^b $\rho=3.270a_0$, $\vartheta=0^\circ$, $\varphi=0^\circ$, $r_{HH}=1.757a_0$, $D_{\infty h}$.

^cCore $(1sa'_1)^2$.

^dCore $(1\sigma_g)^2$.

^eFor the $2^2\Sigma_g^+$ states instead of the outer orbital the weight of the $(1\sigma_g)(1\sigma_u)^2$ configuration is given, see end of Sec. II B.

^fCalculated in similar precision as H_3 .

triangles to obtuse ($\vartheta \rightarrow 180^\circ - \vartheta$) via C_s arrangements. As a rule, except for the ground state surface of H_3 , the potential energy surfaces monotonously decrease along this coordinate from acute to obtuse, or are rather flat. This may be due to the fact that for constant ρ and ϑ the repulsion of the nuclei has its lowest value in the obtuse isosceles triangle.

For given values of the hyperangles the hyperradius ρ is only a scaling parameter not affecting the shape, it is proportional to the leg of the isosceles triangle: $r_{HH} \approx 0.7598 \rho(1 - 0.5 \cos \vartheta)^{1/2}$. As only the parameter ρ determines the size of the triangle, hyperspherical coordinates asymptotically always lead to the three-particle fragmentation limit. Furthermore, as explained in the Appendix, the hyperspherical coordinates exactly correspond to the Dalitz representation used in this paper for the three-particle fragmentation events.

Our discussion is based on *ab initio* CI (configuration interaction) calculations carried out in hyperspherical coordinates and using basis sets which allow one to construct Rydberg wave functions up to $n^* = 3$ [28] and to obtain the correct dissociation products. As CI expansions are slowly converging, these results cannot be as precise as those presented in Ref. [22] although several methods have been applied to prepare sets of optimized orbitals and to efficiently select the configurations. No extrapolation of the results has been applied; they are strictly variational. The calculations have been improved until for several selected points in configuration space the results were stable to within a few times 10^{-4} a.u.; relative energy differences are considered to be

more precise than this value. Only the ground state surface which is well known already has been neglected somewhat in favor of the higher lying states; we expect its precision on the order of 10^{-3} a.u.

Representative energies are given in Table I below. The results are illustrated in the diagrams of Figs. 1–4 as functions of ρ and ϑ , the shapes of the triangles characteristic for each potential energy diagram are shown schematically. Note that in the left and right panels of Figs. 1 and 2 vertical dotted lines indicate coordinates ρ which are common to the central panel at the appropriate angle ϑ . Of course not all possible excited states are shown. In the energy region between the potential curve of the parent ion and the highest curve drawn for the neutral molecule there is an infinite set of higher-lying Rydberg states. The figures show all calculated potentials up to the highest continuous curve obtained (except for a few intruders at energies higher than -1.20 a.u.). In Figs. 3 and 4 three-dimensional plots of the lowest few potential surfaces are presented.

A. The parent ion H_3^+

In its electronic equilibrium the parent ion has the shape of an equilateral triangle with internuclear distances of $1.650a_0$ ($\rho = 2.172a_0$) and a total energy of -1.3438 a.u. [Fig. 1(c)]; the zero point level is at -1.3239 a.u. (-1.3296 a.u. for D_3^+) [29–31]. The electronic structure is a $1^1A'_1$ state with a three-center $1a'_1$ valence orbital. This doubly occupied orbital remains qualitatively unchanged in a large range of

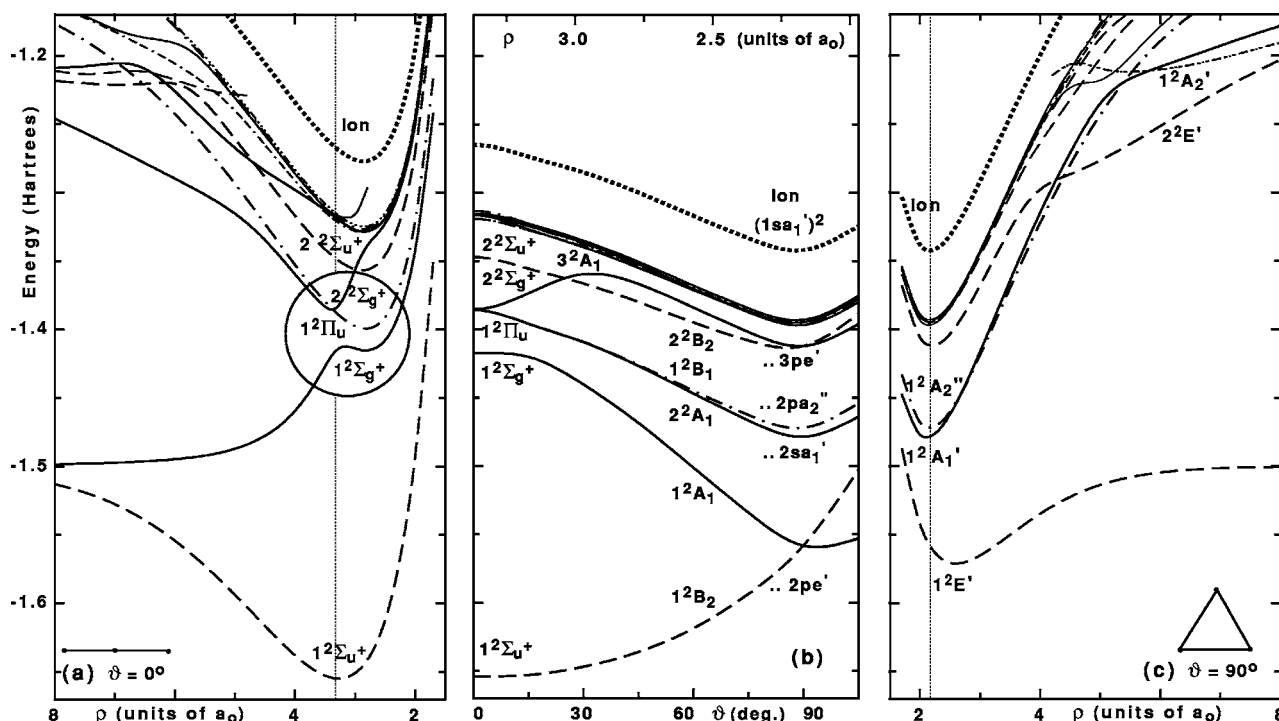


FIG. 1. Cuts through the potential surfaces of H_3 . Left: $D_{\infty h}$ -symmetry; center: transition conserving C_{2v} from D_{3h} to $D_{\infty h}$ (see text); right: D_{3h} . Full lines (in $D_{\infty h}$, C_{2v} , D_{3h}) Σ_g^+ , A_1 , A_1' ; dashed Σ_u^+ , B_2 , E' ; dot-dashed Π_u , B_1 , A_2'' . The vertical lines indicate coordinates common to the middle panel.

nuclear geometries, including the united atom limit Li^+ as well as the lowest dissociation limit H_2+H^+ at -1.1645 a.u. (-1.1674 a.u. for D_2+D^+). Remarkably the dissociation energy of 4.61 eV nearly exactly equals D_e of the H_2 molecule

although here no electron pair must be broken. A particularly distinguished point on the ground state potential surface of H_3^+ is a saddle point in $D_{\infty h}$ symmetry at -1.277 a.u., only about 1.80 eV above the potential minimum, with r_{HH}

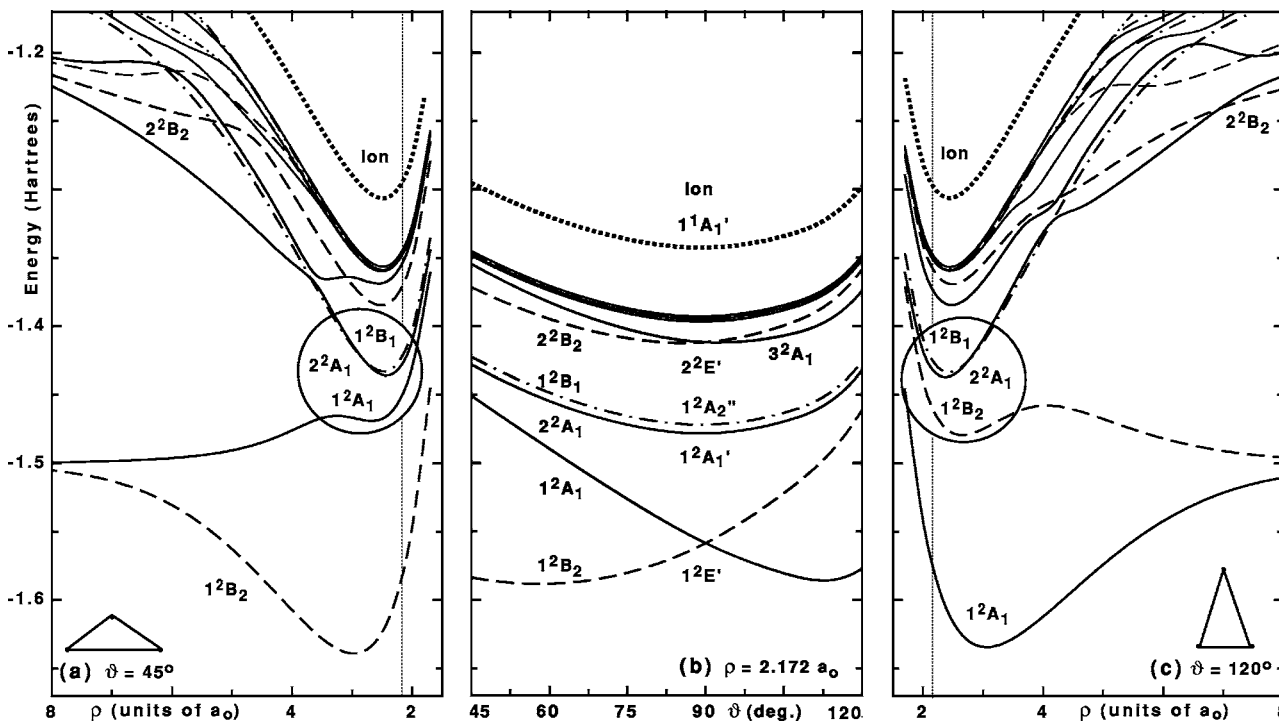


FIG. 2. Cuts through the potential surfaces of H_3 . The center panel shows the effect of a distortion conserving ρ and the C_{2v} symmetry; at left and right the energies of the distorted molecule are shown as functions of ρ (see text). Symbols as in Fig. 1.

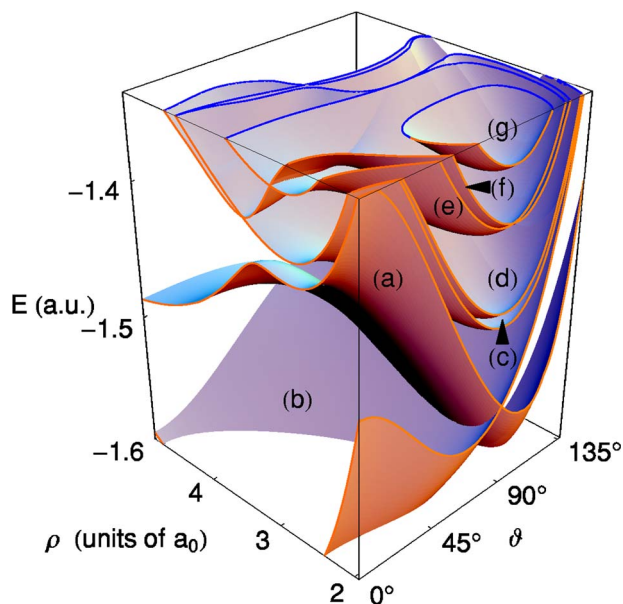


FIG. 3. (Color online) Three-dimensional plot of the lower potential surfaces of H_3 as functions of the hyperspherical coordinates ρ and ϑ (restricted to C_{2v} geometries). The surfaces labeled by (a)–(g) are (a) -1^2A_1 , (b) -1^2B_2 , (c) -2^2A_1 , (d) -1^2B_1 , (e) -2^2B_2 , (f) -3^2A_1 , (g) -4^2A_1 .

$= 1.538a_0$ [$\rho = 2.863a_0$, see the minimum of the ionic curve in Fig. 1(a); a contour plot of the potential well is shown in Ref. [32]]. Deformation in the direction to this saddle point is much more probable than towards dissociation. In fact there are three equivalent saddle points, all leading to the inverted nuclear triangle. At these points a $(1\sigma_g)^2 \cdot 1^1\Sigma_g^+$ electronic wave function is a good first order description.

A second bound state of H_3^+ has linear structure, the $(1\sigma_g)(1\sigma_u) \cdot 3^3\Sigma_u^+$ state with an energy of -1.116 a.u., and $r_{HH} = 2.457a_0$ ($\rho = 4.573a_0$) [33,34] which dissociates at about -1.100 a.u. to $H_2^+ + H$. The orbitals $1\sigma_g$ and $1\sigma_u$ are both valence orbitals; in a localized picture they constitute the two H–H one-electron bonds. At the minimum this surface is 0.085 a.u. (2.3 eV) above the ground state surface. A figure in Ref. [27] shows how at longer interatomic distances several ionic surfaces come close to each other.

From the three $1s$ atomic orbitals of the separated H atoms up to three valence molecular orbitals can be constructed. As the hydrogen atoms approach each other one or two of them are promoted to outer shells and lose their valence character. The united atom Li can be viewed as having one valence (or inner) orbital $1s$, a semivalence orbital $2s$ (or semi-Rydberg, with an effective principal quantum number $n^* = 1.59$) and, beginning with $2p$ ($n^* = 1.96$) pure Rydberg orbitals. At the D_{3h} equilibrium of H_3^+ the $2pe'$ have semivalence character, and in the case of the triplet state the third orbital correlating with the H($1s$) is a promoted $2\sigma_g^*$ orbital.

B. Electronic states of H_3

If the H_3^+ ion captures an electron, neutral H_3 can be formed in a superexcited state with a total energy between -1.324 and -1.164 a.u., depending on the initial state of the

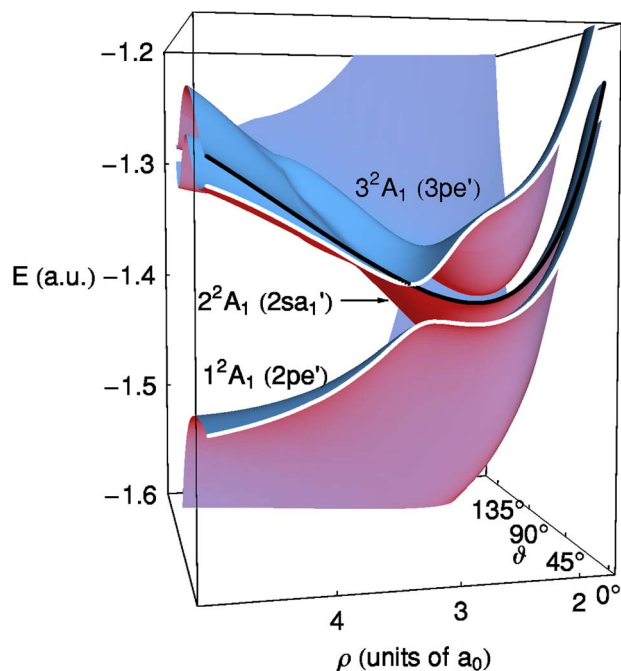


FIG. 4. (Color online) Three-dimensional plot of the three lowest 2A_1 surfaces. The 3^2A_1 surface lies energetically above 2^2A_2 for all C_{2v} geometries. As the system is restricted to $D_{\infty h}$ geometry ($\vartheta = 0^\circ$), relabeling of the associated states induces a crossing of the curves $2^2\Sigma_g^+$ (upper white line) and $1^2\Pi_u$ (black line). The two curves $2^2\Sigma_g^+$ and $1^2\Sigma_g^+$ (upper and lower white line) have an avoided crossing at $\rho \approx 3.4a_0$ [compare Fig. 1(a)].

parent ion and the kinetic energy of the electron. According to “propensity rules” only a small change of the quantum numbers of nuclear motion is to be expected. The superexcited states can decay by emission of radiation or else the internal energy can be redistributed among different degrees of freedom by adiabatic and nonadiabatic processes, eventually leading to the dissociation of the molecule. As far as H_3^+ can be treated as a positively charged closed shell molecule, the electronic states of the neutral system can be characterized by the $n\lambda$ quantum numbers of the Rydberg-like orbital of the outer electron. Here n and l are quantum numbers of the third electron in the united atom and λ gives the irreducible representation of this orbital in the applicable point group. At the D_{3h} equilibrium geometry of the parent ion the orbital sequence of the states relevant for our purposes is $2pe'$, $2sa_1'$, $2pa_2''$, $3pe'$, $3sa_1'$, $3pa_2''$, $3de'$, $3de''$, and $3da_1'$ with total energies between -1.56 and -1.40 a.u. [20,27]. Including degeneracies there are 13 electronic states which belong to the $n=2$ and 3 manifolds of the united atom; they are shown in the Figs. 1(b), 1(c), and 2(b). However, above the $3s$ level the energies are so dense that lettering was impossible. All surfaces except the lowest one have a barrier to linearity. Characteristic energies for two selected geometries are given in Table I. The electronic surfaces may be characterized by the orbital symbol of the outer electron near the equilibrium geometry of H_3^+ . For distorted arrangements it is better to use state labels. In Fig. 1(b) the orbital names as well as the state designations in the C_{2v} and $D_{\infty h}$ symmetries are shown.

If consideration is restricted to the three orbitals correlating with the $H(1s)$ of the separated system ($1sa'_1, 2pe'$ in D_{3h} symmetry), with three electrons one quartet state and eight doublet configurations can be constructed. The two lowest doublets correlate the $H(1s)+H(1s)+H(1s)$ limit at -1.5 a.u. with the ground configuration ($1sa'_1)^2(2pe')$ at equilibrium. These are the only doublet surfaces dissociating to ground state fragments (together with the quartet). Four doublets correlate the excited configuration ($1sa'_1)(2pe')^2$ formally with ionic fragments $H+H^++H^-$ at -1.028 a.u. and two doublets correlate the same limit with $(2pe')^3$. These configurations are carriers of non-Rydberg behavior.

The figures show that in general the curves are parallel to the potential of the parent ion for short and intermediate distances, exhibiting their Rydberg nature, and have an absolute potential minimum at the same geometry or very close. The most important exceptions are parts of the Jahn-Teller split $2pe':^2E'$ ground state surface. At the equilibrium geometry of H_3^+ the $2pe'$ have an effective principal quantum number of $n^* = 1.52$ and hence have semi-Rydberg character. Another exception can best be explained in D_{3h} symmetry. In Fig. 1(c) we see that for $\rho > 4a_0$ the slopes of the curves $2^2E', 1^2A'_1$, and $1^2A'_2$ are much flatter than that of the parent ion. These are the components of the $(1a'_1)(1e')^2$ configuration having ion pair electronic structure and thus long-range attractive interactions of the fragments. These states, called “V states” by Mulliken [35], correspond to the B and F states of the H_2 molecule with their wide potential wells [64]. The phenomenon is of course not restricted to D_{3h} symmetry; we see the slopes of these “ion pair” potentials also in other figures; in Fig. 2(a) the onset (the anticrossing of 2^2A_1 and 3^2A_1) is as low as -1.36 a.u. One component of this configuration has been reported in 1979 by Kulander and Guest [36]. At intermediate to long distances ρ there is a continuous exchange of properties between these states and the wave function of the ground state which acts like an avoided crossing.

In linear geometry most of the states retain $(1\sigma_g)^2(nl\lambda)$ electronic structure at not too large internuclear separation, but because of the elongated shape of the molecule there is considerable $s-d\sigma$ mixing such that l ceases to be a good quantum number. Furthermore, and more important, there is an additional $2^2\Sigma_g^+$ valence configuration with a $(1\sigma_g)(1\sigma_u)^2$ leading determinant, correlating with $(1s)(2p_0)^2$ in the united atom and having the core of the $3^2\Sigma_u^+$ state of the parent ion. In $D_{\infty h}$ symmetry this configuration anticrosses all $2^2\Sigma_g^+$ curves from high energies close to the united atom to the $3H(1s)$ limit at -1.5 a.u. for long distances [see Fig. 1(a)], adding a strongly repulsive state to the energy diagram. The effect is most pronounced for $D_{\infty h}$ symmetry (because this is the equilibrium geometry of the triplet state of H_3^+). For non-linear geometries this interaction manifests itself as an anticrossing of the 2^2A_1 and 3^2A_1 surfaces [see Fig. 2(a)]; the reduced slope is responsible for the curtainlike puff of the surfaces 2^2A_1 and 3^2A_1 , visible at the top of Fig. 3 for $\rho \approx 4$.

C. The surfaces of $2pe'$

The first two surfaces, 1^2A_1 and 1^2B_2 in C_{2v} symmetry, $1^2A'$ and $2^2A'$ in C_s , constitute a pair of two sheets of a

surface which is penetrating itself in D_{3h} symmetry (i.e., adiabatic transitions between the sheets are possible above -1.57 a.u.). The surfaces are repulsive and lead either to the fragments H_2+H at -1.674 a.u. or to three $H(1s)$ at -1.500 a.u. All three-particle dissociation processes at energies below -1.125 a.u. [one $H(n=2)$ atom] and also the processes producing two fragments at energies below -1.290 a.u. [$H(n=2)+H_2$ at the zero point level] move on one or both of these two surfaces.

The lower component of the $2pe'$ surfaces has been computed carefully long ago [10,11] for the study of the isomerisation reaction of $H+H_2$ [12]. The minimum of the lowest curve in Fig. 1(a) corresponds to the saddle point in linear geometry of the ground state surface; the surface is repulsive and leads to dissociation as soon as the symmetry is reduced to $C_{\infty v}$. The second set of energies in Table I refers to this point.

Recently Abrol *et al.* [37] have calculated matrix elements for the nonadiabatic coupling of the lowest two surfaces. From the behavior of the topological phase they conclude that there are conical intersections or avoided crossings of the second ($2pe'$) and the third surface ($2sa'_1$). At lower energies the $2pe'$ states do not cross a higher surface. There is however, an intersection at short interatomic distances. In D_{3h} symmetry $2sa'_1$ penetrates $2pe'$ for $r_{HH}=0.94 a_0$ ($\rho = 1.24 a_0$) at an energy of -1.23 a.u. [This crossing point can be anticipated because in the united atom Li the ground state has the configuration $(1s)^22s$; we have not investigated the conical intersections in C_{2v} symmetry emanating from this point.] Furthermore, from the potential curves of H_2 tabulated by Kolos and Wolniewicz [38] we see that near $r_{HH} = 1.45a_0$, in the limit of the two-fragment dissociation, the curve corresponding to $H_2b^3\Sigma_u^+ + H(1s)$ is degenerate with the curves of $H_2X^1\Sigma_g^+ + H(n=2)$ at -1.298 a.u. (A figure explaining this situation is shown in Ref. [27].) In fact the repulsive curve of the b state crosses the H_2 potential at the bottom, below the lowest vibrational level. This intersection has a continuation to finite distances between H and H_2 . Because of their high energy both these adiabatic dissociation channels need not be considered for the experiments presented in this study; they may be accessible for fast electrons captured by vibrationally hot H_3^+ .

D. The surfaces of $2sa'_1$ and $2pa''_2$

The third and fourth surfaces, 2^2A_1 and 1^2B_1 in C_{2v} , $3^2A'$ and $1^2A''$ in C_s symmetry, are the first two which have an absolute minimum for the undissociated molecule [Figs. 1(c) and 3]. The vibrational levels of the $2sa'_1$ state have been reported in Ref. [27]. In the lower part of the potential well the two surfaces are very close to each other (≈ 100 meV), like twins, and separated from the higher surfaces. The two surfaces become degenerate components of the lowest $2^2\Pi$ state in linear symmetry. As the $2s$ orbital is transformed into the in-plane π component and at the same time the $3pa_1$ orbital of the next higher state becomes a σ_g orbital in the linear molecule, a strong exchange of orbital angular momentum among the first three 2^2A_1 states occurs, as apparent for small values of ϑ in Figs. 1(b) and 4.

At energies below -1.4 a.u. no adiabatic transition to other surfaces is possible from these surfaces; only nonadiabatic effects can dissociate the H_3^* system. However, as can be seen at left and right in Fig. 2(b), if the equilibrium geometry is distorted to C_{2v} one of the ground state surfaces comes rather close; 1^2A_1 for obtuse triangles ($\vartheta < 90^\circ$) and 1^2B_2 for acute triangles ($\vartheta > 90^\circ$). The encircled parts in Figs. 2(a) and 2(c) show two situations where nonadiabatic coupling of 2^2A_1 and 1^2B_1 with the neighboring ground state surface is strong because the wavelengths of the wave functions of nuclear motion are similar; hereby also a connection of the geometry of the molecule and the symmetry of the coupling is suggested. Indeed vibrational coupling rapidly predissociates the $2sa'_1$ rovibrational levels ($\tau \approx 200$ fs [39]). By contrast the $3sa'_1$ levels are much further removed from the ground state surface and relatively long lived ($\tau \approx 1$ ns [40]).

E. The surfaces of $3pe'$

The two components 3^2A_1 and 2^2B_2 of $3pe'$ ($4^2A'$ and $5^2A'$ in C_s symmetry) are also largely separated both from lower and from higher states, at least at total energies up to -1.35 a.u. and not too close to linear arrangement. In contrast to the $2pe'$ states, the sheets of $3pe'$ penetrate each other not only in D_{3h} symmetry; further crossing points which give rise to conical intersections can be seen in Figs. 1(a), 1(b), and 2(a). Again for not too large values of ρ the curves are parallel to the ion. A notable exception is the barrier of 3^2A_1 visible in Fig. 1(b) separating the D_{3h} and linear arrangements. This is in fact a saddle point [see Figs. 2(a) and 4] at $\vartheta = 40^\circ$, $\rho = 2.8a_0$, with an energy of -1.367 a.u. only 1.33 eV above the D_{3h} minimum, leading to a 0.60 eV deep "potential basin" in linear geometry [Figs. 1(a) and 3]. The minimum of this basin at -1.388 a.u. is only 0.73 eV above the absolute minimum; for no other surface is the barrier to linearity as shallow as for the 3^2A_1 state. Furthermore, in $D_{\infty h}$ symmetry the $2^2\Sigma_g^+$ potential curve is crossed by $1^2\Pi_u$ at the bottom of the basin [see Figs. 1(a) and 4].

The reason for this basin is the additional $2^2\Sigma_g^+$ state mentioned in Sec. II B which forces the third adiabatic 2^2A_1 surface to bend down as quasilinearity is approached [Fig. 1(b)] and the fact that the third surface asymptotically correlates with an excited dissociation limit. This situation is shown inside the circle of Fig. 1(a). There we observe also an avoided crossing of the first two $2^2\Sigma_g^+$ curves with a wide energy separation of 0.9 eV, indicating strong nonadiabatic effects. A H_3^* molecule arriving in this region may tunnel forth or back to the deeper potential well. It can find an adiabatic way to the 2^2A_1 surface (the lower component of the $1^2\Pi_u$ state) or it can couple nonadiabatically to the dissociative 1^2A_1 surface.

Kokoouline and Greene (Ref. [24] and references cited therein) have studied the dynamics of the fragmentation processes of excited H_3 molecules formed in dissociative recombination. In their model the $3pe'$ states and the next higher $3s$ state play an important role, however, solely in the immediate vicinity of the ionic minimum at D_{3h} geometry.

F. Higher surfaces

At the H_3^+ equilibrium geometry about 3000 cm^{-1} above the $3pe'$ level seven electronic states follow within an interval of about 800 cm^{-1} , from $3sa'_1$ to $3da'_1$ with minima between -1.401 and -1.398 a.u. The next higher state $4pe'$ (not shown here) is then separated by nearly 4000 cm^{-1} . These states are represented as an unresolved band, e.g., in Fig. 1(b); only the lowest $3sa'_1$ surface is shown in Fig. 3. The figures suggest that this situation does not change essentially upon distortion of the geometry for total energies below -1.3 a.u. Note that the zero point energies in these potentials typically are 4500 cm^{-1} (4747 cm^{-1} for the $2s$ state [27], 4361 cm^{-1} for H_3^+ [32]). There is little hope to understand the dynamical transitions within this group of states, but the whole group is clearly separated from the lower surfaces avoiding any adiabatic connection. Just as the $2pe'$ surfaces approach $2s$ (Sec. II D), the $3pe'$ surfaces come closer to $3s$ for C_{2v} distorted geometries [see the distance between the sixth and seventh curve in Fig. 2(b)]. But in this case the nonadiabatic coupling does not lead directly to a repulsive surface.

III. EXPERIMENTAL PROCEDURE

In our experiment we monitor the dissociation of individual, state-selected H_3^* molecules and determine the three atomic momentum vectors of reaction (1) in coincidence. This technology has been described in detail in previous publications [41–44]. The state preparation involves metastable triatomic hydrogen molecules which are produced in a fast (3 keV) beam by charge transfer neutralization of H_3^+ . The rotationless level of H_3 $2pa''_2$ is immune to rapid predissociation [45] and is present in the neutral beam in a range of vibrational levels (v_1, v_2). In this notation v_1 and v_2 describe the symmetric stretch and degenerate bending mode vibrational quantum numbers. Photoexcitation spectra of the metastable levels in H_3 and D_3 have been studied in great detail [46–49] and firm electronic, vibrational, and rotational assignments of the spectra have emerged, backed by MQDT theory based solely on *ab initio* parameters [22].

The metastable vibrational levels are used in our experiment to photoexcite H_3^* molecules in well-known quantum states. The excitation is carried out inside the cavity of a narrow band dye laser, which is tuned to specific absorption transitions. Due to the state-selective excitation, the total energy of the molecule, W , measured relative to three separated ground state hydrogen atoms is precisely defined in our experiment.

The fast H_3 molecules spend ≈ 1 ns in the laser interaction region. They typically predissociate on time scales faster than 10 ns [50], their center of mass propagating at an energy of 3 keV towards the detector. The photofragments separate spatially from this direction according to their transverse momentum. They are detected in coincidence using position- and time-sensitive multihit-detectors [42]. For the current work, the free-flight distance to the detector was extended to 230 cm. This enabled us to record three-body decay from the lowest bound states of H_3 for which the total energy release in reaction (1) is as low as 800 meV. Over this flight dis-

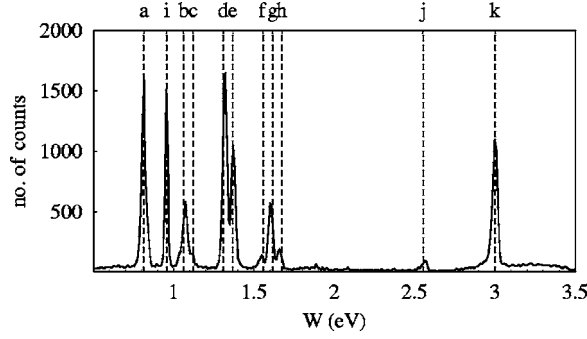


FIG. 5. Typical kinetic energy spectrum observed after photoexcitation of the $3sa'_1(0,0)$ level of D_3 . The dashed lines (a-k) indicate the expected position of particular states. These states are as follows: a, $2sa'_1(0,0)$; b, $2sa'_1(0,1)$; c, $2sa'_1(1,0)$; d, $2sa'_1(0,2)$; e, $2sa'_1(1,1)$; f, $2sa'_1(0,3)$; g, $2sa'_1(1,2)$; h, $2sa'_1(2,1)$; i, $2pa''_2(0,0)$; j, $3pe'(0,0)$; k, $3sa'_1(0,0)$.

tance, the atomic fragments separate in space by as much as 50 mm. Fast electronic signal-processing permits to measure the spatial coordinates of the neutral fragments with a resolution of $<100 \mu\text{m}$ and the arrival time differences with a resolution of $<100 \text{ps}$. This information is used online to distinguish triple coincidences of process (1) from false coincidences produced by fragments of reaction (2). For each triple coincidence event, the momentum vectors $\{\vec{k}_1, \vec{k}_2, \vec{k}_3\}$ in the center-of-mass frame are evaluated from the time and position information [42,43].

In addition to direct radiative excitation of a specific vibronic level, we observe the population of lower lying Rydberg states by radiative cascade from the photoexcited levels. This process is recognized in the kinetic energy spectra of the three correlated fragments

$$W = \frac{1}{2m} (|\vec{k}_1|^2 + |\vec{k}_2|^2 + |\vec{k}_3|^2) \quad (3)$$

(m being the hydrogen mass). An example is shown in Fig. 5 which gives a three atom energy spectrum observed after photoexcitation of the $3sa'_1(0,0)$ level of D_3 .

The assignment of the predissociated states which appear in Fig. 5 (as well as in similar spectra following photoexcitation of $3de''$ and $3da'_1$ levels) is based on the previously known energy levels collected in Tables II and III. We observe that population of low-lying electronic states via radiative transitions occurs frequently for D_3 , quite in contrast to H_3 . This is caused by a mass-dependent weighting of the dissociation reaction. As nonradiative dissociation is triggered by nonadiabatic couplings, it is suppressed in favor of radiative transitions if the nuclei are heavier. The great variety of vibrational levels populated in radiative transitions to the $2sa'_1$ states of D_3 presumably results from the fact that the bond length of the $2sa'_1$ state ($r_{\text{HH}}=1.606 a_0$) differs significantly from its radiative parent $3pe'(r_{\text{HH}}=1.680 a_0)$ [39,51]. Vibrational transitions in the electronic transition $3pe' \rightarrow 2sa'_1$ of D_3 have also been observed by Herzberg *et al.* [51].

TABLE II. Absolute state energies in D_3 (experimentally determined).

State ^a	Energy in a.u. ^b	Energy in eV ^c
$D+D_2(v=0, N=0)$	-1.6674	-4.556
$D+D+D$	-1.5	0
$D_3 2sa'_1(0,0)^{d,e}$	-1.470	0.81
$D_3 2sa'_1(1,0)^{j,e}$	-1.459	1.10
$D_3 2sa'_1(0,1)^{j,e}$	-1.461	1.05
$D_3 2pa''_2(0,0)^e$	-1.466	0.94
$D_3 2pa''_2(1,0)^{f,e}$	-1.455	1.23
$D_3 2pa''_2(0,1)^{f,e}$	-1.457	1.17
$D_3 3pe'(0,0)^{g,e}$	-1.406	2.55
$D_3 3pe'(1,0)^{j,e}$	-1.396	2.83
$D_3 3pe'(0,1)^{j,e}$	-1.398	2.77
$D_3 3sa'_1(0,0)^{h,e}$	-1.390	2.99
$D_3 3de''(0,0)^{i,e}$	-1.387	3.09
$D_3 3de''(1,0)^{f,e}$	-1.376	3.37
$D_3 3da'_1(0,0)^{i,e}$	-1.386	3.10
$D_3^+ 1^1A'_1(0,0)^e$	-1.331	4.60

^aAll atomic states refer to the $D(1s)$ ground state. The molecular states refer to the lowest rotational level in each state and use the state designation (v_1, v_2) .

^bRelative to $D^++D^++D^++3e$.

^cRelative to $D+D+D$.

^dBased on [52].

^eAll these values have a systematic uncertainty of ± 0.001 a.u. due to the uncertainty of the absolute energy of $2pa''_2(0,0)$ [44,53]. Differences between these levels are known with much higher precision. The values have been related to the values of H_3 by a correction for the vibrational and rotational zero-point energies of $2pa''_2(0,0)$ [49,52,54] and $1^1A'_1(0,0)$ [30,32].

^fBased on [49].

^gBased on [52].

^hBased on [39].

ⁱBased on [55].

^jBased on estimation in [51].

We use the total energy W determined for each single coincidence event from Eq. (3) to attribute the data $\{\vec{k}_1, \vec{k}_2, \vec{k}_3\}$ of the event to a specific predissociated state. Typically data sets containing at least 10^3 events for each particular level are collected. We represent the correlation of the fragment momentum vectors \vec{k}_i using momentum correlation maps (Dalitz plots, see the Appendix), after accounting for the geometric detection efficiency [43,44].

IV. EXPERIMENTAL RESULTS

To date we have recorded momentum correlation maps for more than 30 vibronic states of H_3 and D_3 . These include directly photoexcited levels in the $(3sa'_1, 3de'')$ states as well as levels in the $(3pe', 2pa''_2, 2sa'_1)$ states, which are populated by radiative cascade. Nearly all states have been observed in the vibrational ground state as well as in vibrationally excited states. The $2sa'_1$ state of D_3 has been studied over a

TABLE III. Absolute state energies in H_3 (experimentally determined).

State ^a	Energy in a.u. ^b	Energy in eV ^c
$H+H_2(v=0, N=0)$	-1.6645	-4.478
$H+H+H$	-1.5	0
$H_3 2sa'_1(0,0)^{d,e}$	-1.464	0.97
$H_3 2pa''_2(0,0)^e$	-1.460	1.09
$H_3 2pa''_2(1,0)^{f,e}$	-1.445	1.49
$H_3 2pa''_2(0,1)^{f,e}$	-1.448	1.41
$H_3 3pe'(0,0)^{g,e}$	-1.401	2.69
$H_3 3pe'(0,1)^{i,e}$	-1.389	3.01
$H_3 3sa'_1(0,0)^{h,e}$	-1.384	3.15
$H_3 3sa'_1(1,0)^{h,e}$	-1.369	3.55
$H_3 3sa'_1(0,1)^{h,e}$	-1.372	3.48
$H_3 3de''(0,0)^{h,e}$	-1.381	3.23
$H_3 3de''(1,0)^{h,e}$	-1.367	3.62
$H_3 3de''(0,1)^{h,e}$	-1.370	3.54
$H_3 3da'_1(0,0)^{g,e}$	-1.380	3.26
$H_3^+ 1^1A'_1(0,0)^{f,e}$	-1.325	4.75

^aAll atomic states refer to the $H(1s)$ ground state. The molecular states refer to the lowest rotational level in each state and use the state designation (v_1, v_2) .

^bRelative to $H^+ + H^+ + H^+ + 3e$.

^cRelative to $H+H+H$.

^dBased on [52].

^eAll these values have a systematic uncertainty of ± 0.001 a.u. due to the uncertainty of the absolute energy of $2pa''_2(0,0)$ [44,53]. Differences between these levels are known with much higher precision.

^fBased on [54].

^gBased on [55].

^hBased on [5].

ⁱBased on [50].

particularly wide range of vibrational excitation, reaching up to $v_1=3$ or $v_2=3$. The total energy release W varies from 0.8 to 3.6 eV for the levels studied. Rotational quantum numbers are well-known for nearly all the directly photoexcited levels. For levels populated by radiative cascade, some ambiguity exists about their rotational excitations ($\Delta N=0, \pm 1$). This means that the data from momentum correlation maps of the states ($3pe'$, $2pa''_2$, $2sa'_1$) include up to four low-lying rotational levels in unspecified proportion [65].

The momentum correlation maps indicate the final-state distribution of process (1) in terms of the relative arrangement of the fragment momentum vectors in the dissociation plane. Figure 6 illustrates the meaning of the momentum correlation map. The scale of the Dalitz plot is energy-normalized. Due to momentum conservation, all experimental data values fall inside a circle of radius $1/3$. In some experimental plots small blank patches appear at the edge of the round area. This indicates that the geometric detection efficiency and specific energy release prevented recording data in these areas of the maps.

Our experimental results are collected in Figs. 7–10. The maps show highly structured patterns in some cases while

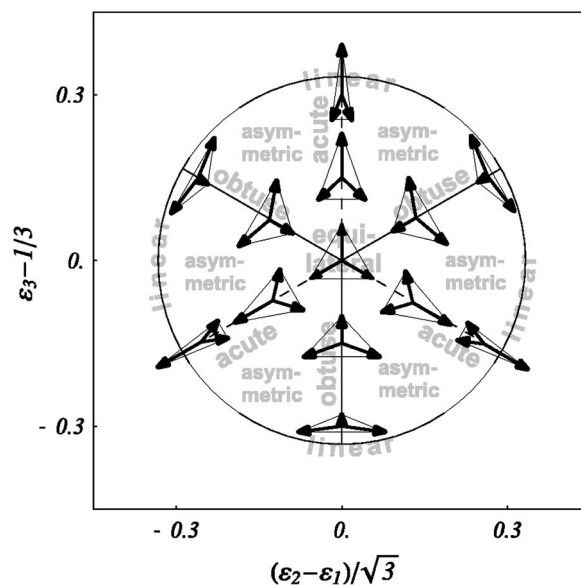


FIG. 6. Momentum configurations in the Dalitz plot. The coordinates depend on the fragment momenta $\epsilon_i = |\vec{k}_i|^2 / (2mW)$. The orientation and the magnitude of the momentum vectors is indicated by arrows. Each triangle represents a configuration in momentum space.

they are relatively simple in other cases. An apparent criterion for the complexity of the correlation map is the total energy W and the degree of excitation of the degenerate bending mode vibration. The momentum correlation maps of the lowest energy states are generally low-structured ($2pa''_2, 2sa'_1, 0.8eV \leq W \leq 2.0eV$) indicating a single or a few

$D_3 2sa'_1(v_1, v_2)$

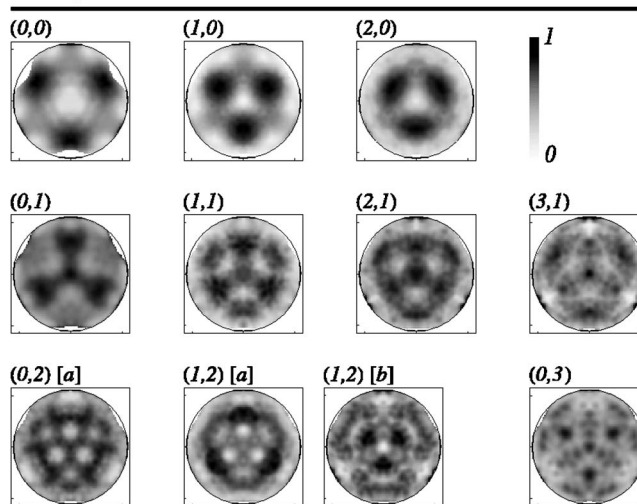
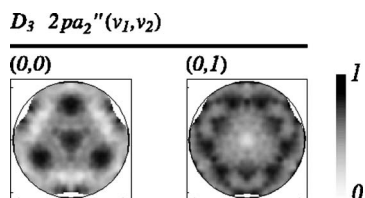


FIG. 7. Momentum correlation maps of $D_3 2sa'_1$ states. The two plots $(1,2)[a]$ and $(1,2)[b]$ originate from data sets obtained after photoexcitation of $3sa'_1(0,0)$ ($[a]$) and $3de''(0,1)$ ($[b]$). Presumably, the two appearing structures indicate that in one case an $l=0$ and in the other case an $l=\pm 2$ vibrational state is primarily populated by the respective radiative transition (l being the vibrational angular momentum quantum number). Usually, data sets assigned to equal vibronic states result in the same correlation pattern, though the radiative parents of these states might be different.

FIG. 8. Momentum correlation maps of D_3 $2pa_2''$ states.

isolated islands of preferred orientation of the fragment momentum vectors (see Figs. 7–9). The energetically higher-lying states $3sa_1'$, $3de''$, $3pe'$ ($2.6\text{eV} \leq W \leq 3.6\text{eV}$), on the other hand, all appear highly structured (see Fig. 10). This fact will be discussed in more detail in Sec. V. We first focus on the rather simple patterns in the momentum correlation maps of $2pa_2''$ and $2sa_1'$ states.

A. Vibrational levels in the $2sa_1'$ and $2pa_2''$ states

When examining the maps of the vibrationally excited $2sa_1'$ states of D_3 (see Fig. 7), similarities between states with the same bending-mode quantum number v_2 can be identified. The states with $v_2=0$ (top row in Fig. 7) show remarkably simple maps. They are characterized by three pronounced maxima, which are equivalent due to particle-exchange symmetry of the Dalitz plot. A comparison with Fig. 6 shows that these maxima correspond to a momentum orientation in the form of an obtuse-angled, isosceles triangle. As the symmetric stretch mode is excited ($v_1=1, 2$) the maximum contracts towards the center of the map. A weaker feature in these maps indicates that acute-angled, isosceles geometries are also present. Near the equilateral triangle configuration in the center of the plot, the density tends to zero, which means that the geometry of equal momentum sharing is highly restricted in this case.

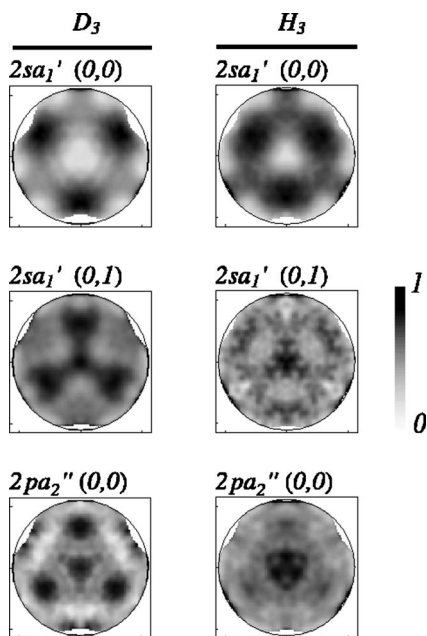
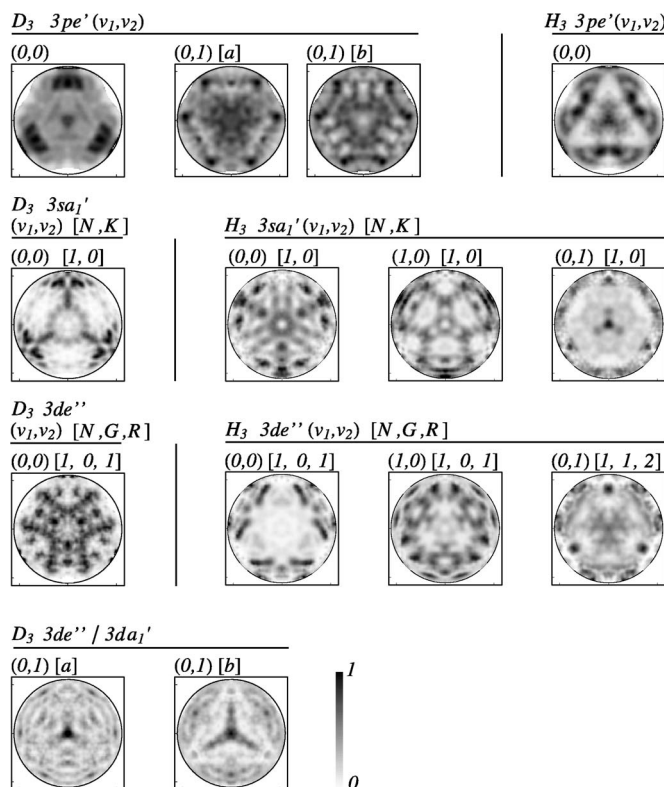
FIG. 9. Isotope effects in the $2sa_1'$ and $2pa_2''$ states. Here, similarities between D_3 and H_3 structures are obvious.

FIG. 10. Compilation of momentum correlation maps of the energetically higher states of D_3 and H_3 . Well-known rotational quantum numbers are indicated in square brackets. The two plots in the last row can be assigned to rotational levels of $3de''(0,1)$ as well as $3da_1'(0,1)$. The additional lettering [a] and [b] indicates that the states [a/b] of the last row are the respective radiative parents of the two D_3 states $3pe'(0,1)[a/b]$ in the first row. Most likely, rotational levels are differently occupied in these transitions, which leads to a visible structural difference in the two plots $3pe'(0,1)[a]$ and $3pe'(0,1)[b]$.

States with one quantum of excitation in the vibrational bending mode ($v_2=1$) show slightly more complicated structures. In contrast to the $2sa_1'$ states with $v_2=0$, a maximum appears at the center of the map and dominant contributions appear at acute-angled configurations. Certain obtuse-angled configurations also appear, as if a portion of the corresponding map in the first row ($v_1, v_2=0$) were added. These are variably emphasized for each value of v_1 . Also in this row the features appear to contract towards the center as the energy increases. For $v_2=2$, the structures gain further complexity. Clear similarities can be found for the two states denoted by $(0,2)[a]$ and $(1,2)[a]$.

Two levels of the $2pa_2''$ state of D_3 were investigated (see Fig. 8). For the vibrational ground state, the structure is again very simple. But in contrast to the corresponding map of the $2sa_1'$ -state, distinct maxima appear at acute-angled geometries as well as a smaller maximum at the equilateral triangle configuration. Now the lowest density is at obtuse-angled geometries. Also here the structure for $(v_1=0, v_2=1)$ is more complex than that of the vibrational ground state. Again in contrast to the corresponding map of the $2sa_1'$ state, where a bending mode excitation changes the density in the

center from zero to a maximum, now the maximum turns into a minimum for $2pa_2''$ ($v_1=0, v_2=1$).

Comparing the results for D_3 with those for H_3 (Fig. 9), it may be noted that the patterns in the maps for the states $2sa_1'$ and $2pa_2''$ are definitely similar. In particular for $2sa_1'(0,0)$, the structure is virtually the same, but slightly more contracted for H_3 . This effect is also seen in the two $2sa_1'(0,1)$ maps. The only vibrationally excited $2sa_1'$ level of H_3 , which we investigated, shows basically the same structure that appears in the various $2sa_1'(v_2=1)$ states of D_3 (compare Fig. 7). It appears that the smaller nuclear mass modifies the correlation pattern in a manner that the map features contract towards the center, quite similar to what is observed when the total energy is increased. This effect is most pronounced in the first two rows of Fig. 7.

Matters are much more complicated when one tries to discuss the relevant features of the momentum correlation maps of the energetically higher-lying $n=3$ states.

B. The states $3pe'$, $3sa_1'$, and $3de''$

These states lie in the energy range $2.6 < W < 3.6$ eV. Their momentum correlation maps are in general very complex and fine structured (see Fig. 10). Very dissimilar maps appear for the two isotopes, H_3 and D_3 . In contrast to the situation for the $n=2$ states, maps of levels which only differ by the excitation of the symmetric vibrational mode (v_1) show only marginal similarities. The only rule that seems to hold in nearly all situations ($n=2$ and $n=3$ states) is that a bending mode excitation changes a minimum in the center of the plot to a maximum and vice versa. Once again, the total energy W of the state is a gauge for the richness of the structures (compare Tables II and III).

There are two plots which reveal an influence of rotation on the momentum correlation. These are the plots of the D_3 states $3pe'(0,1)[a]$ and $3pe'(0,1)[b]$ (top row in Fig. 10). As these states are populated by radiative transitions from different upper states (type $[a]$ and $[b]$ in the bottom row of Fig. 10), the data of each plot contains up to three rotational levels. Though the patterns of $3pe'(0,1)[a]$ and $3pe'(0,1)[b]$ are to some extent similar, distinct differences occur in the finer structures of these plots. This leaves no other interpretation than a different distribution of rotational levels, affected by different radiative parents.

V. DISCUSSION

The most remarkable feature in our experimental momentum correlation maps for process (1) is the appearance of simple, regular structures in the maps of $2sa_1'$ and $2pa_2''$ states, while the maps of all energetically higher states are without apparent regularity and are highly structured. This section aims to interpret these differences in a qualitative manner by pointing out fundamental differences in the dissociation pathways for low-lying states ($W \leq 2$ eV) and higher lying states ($W > \approx 3$ eV). We now get back to the results of Sec. II.

The potential energy surfaces of all Rydberg states investigated here have deep potential minima near the equilibrium

geometry of the ion (see Fig. 1). All these surfaces converge to dissociation limits with at least one excited fragment, at energies much higher than the dissociated levels investigated here. As a consequence dissociation to $H(1s)+H(1s)+H(1s)$ or $H(1s)+H_2(v, J)$ has to occur via the ground state surfaces. We note here again that the ground state surface does not cross the respective Rydberg state surfaces at nuclear geometries where the dominant contribution of the vibrational wave function of the predissociated state is centered.

In order to exit from the bound molecular Rydberg state into the three-particle continuum at least one nonadiabatic process has to be involved. As discussed already in Sec. II D the states $2sa_1'$ and $2pa_2''$ are embedded in the two sheets of the electronic ground state surface $2pe'$ with not too dissimilar oscillation periods in the ground state and the Rydberg state nuclear wave functions. For these states dissociation can occur by direct coupling. The coupling between $2sa_1'$ and $2pe'$ is mediated by the degenerate vibrational mode v_2 , while $2pa_2''$ can couple to $2pe'$ via rotation [39]. Very likely, the difference in coupling is responsible for the different correlation maps for $2sa_1'$ and $2pa_2''$ states with identical vibrational excitation [6]. It is quite comprehensible that the $2sa_1'$ -correlation structure only depends on the excitation of the v_2 -vibrational mode, as the v_1 vibration cannot trigger a transition because of symmetry arguments [39].

Generally, the dissociation can also proceed in a sequence of nonadiabatic transitions to intermediate surfaces before reaching the ground state. In addition to symmetry requirements, the strength of such couplings is ruled by two factors: (a) the magnitude of the coupling term itself and (b) the overlap of nuclear wave functions. Factor (b) generally decreases with an increasing energy gap between the surfaces involved, due to dissimilar nuclear-motion wave functions. Both factors influence the final state contribution. In a previous publication [56], we demonstrated how factor (b) can affect the momentum correlation in a direct transition to the ground state.

The magnitude of nonadiabatic coupling terms [factor (a)] is regulated by the variation of the electronic wave function amplitudes with the nuclear coordinates [23]. If electronic wave functions change rapidly with the motion of the nuclei, the coupling is generally strong. This situation occurs when the two potential surfaces approach each other in an avoided crossing. The character of the electronic wave function changes dramatically when the nuclei pass through such a configuration on the adiabatic sheet. In cases like this the adiabatic representation competes with the diabatic representation, which introduces a basis set of smoothly changing electronic wave functions leading to a crossing of the respective diabatic potentials [14,57].

In Sec. II E we have pointed out that an additional potential basin of 3^2A_1 at linear geometry has an avoided crossing with 1^2A_1 at its bottom (Fig. 4). In this region the coupling to the continuum is strong. The linear geometry is separated from the D_{3h} equilibrium geometry of the $3pe'$ surface 3^2A_1 by a potential barrier at $W \approx 3.6$ eV. Hence, tunneling enables the vibrational levels of $3pe'$ to access the basin at linear geometry and to reach the continuum. The consequence is, that not only the $3pe'$ state is efficiently coupled

to the continuum. It may also enhance the dissociation rate of any energetically higher state by acting as an intermediary on the way to the continuum. As the energy separation of the higher $n=3$ sheets to 3^2A_1 is much smaller ($\Delta W \approx 0.5$ eV) than to the ground state surfaces ($\Delta W \geq 3.0$ eV), nonadiabatic transitions to 3^2A_1 are of much higher probability than those directly to the ground state. The fact that 3^2A_1 has such an efficient coupling to the 1^2A_1 continuum makes the dissociation process via 3^2A_1 certainly competitive with the direct nonadiabatic transition to the ground state [66].

The conclusion is, that for the $n=3$ states at least two different dissociation channels are possible, while for $n=2$ states only the direct coupling to one of the ground state surfaces has to be invoked. This difference may be held responsible for the clear differences which appear in the momentum correlation maps of $n=2$ and $n=3$ states. The rather simple correlation structures of $n=2$ apparently arise from a simple dissociation mechanism, when the Rydberg state couples directly to one of the ground state sheets. The complex correlation maps of the $n=3$ states are most likely the consequence of more complicated dissociation pathways, where the initial wave function is transformed in several steps. It is conceivable that along this landscape of different electronic configuration, multiple paths lead to the same final states and hence quantum interference imprints complex features in the correlation maps.

VI. CONCLUSIONS

Our quantum-chemical calculations show that an additional dissociation pathway to the continuum exists for excited states of H_3 with $W \geq 3$ eV. In accordance with this we observe in our experiment a fundamental change in the fragment momentum correlation for states which lie energetically above this threshold. The increase in complexity for the momentum correlation maps above this threshold is likely due to the increased number of nonadiabatic coupling pathways and interference between these paths.

This is one important step for the interpretation of the presented momentum correlation structures. Further theoretical efforts have to be undertaken to evaluate the huge amount of information encoded in the momentum correlation plots. The correlation structures of the $n=2$ states are predestined to contribute significantly to the knowledge of nonadiabatic couplings in this molecule and in general. To filter out information about the nonadiabatic operator from the correlation data, one has to take into account that also the wavepacket propagation on the ground state sheets effects the momentum correlation. A calculation that traces back the momentum configurations in the final state to a spatial distribution of the nuclear wave function a short time after the coupling to the ground state ceased might clarify at which nuclear geometries the coupling occurs.

An interpretation with respect to symmetry arguments is also desirable. Recently, theoretical investigations by Walter focused on the three-body fragmentation of H_3 s -Rydberg states with rotational quantum numbers ($N=1, K=0$) and nuclear spin $S_N=3/2$ [58]. One result of Walter's work is that the momentum configuration of equal momentum sharing

(center of the Dalitz plot) is forbidden due to symmetry restrictions. This is in agreement with our data. Furthermore, we suppose that a general rule exists for the accessibility of the total symmetric momentum configuration. Most likely, the quantum numbers L and ν_2 play a decisive role. The rule

$$L + \nu_2 = \text{even} \rightarrow \text{symmetric configuration forbidden,}$$

$$L + \nu_2 = \text{odd} \rightarrow \text{symmetric configuration allowed}$$

holds for all investigated states of H_3 and for nearly all states of D_3 . We are confident that a deeper analysis of symmetry restrictions will state this rule more precisely.

Uncovering and understanding the dissociation channels of H_3 Rydberg states is of substantial importance for the explanation of their lifetimes and the rate of dissociative electron capture of H_3^+ in the diffuse interstellar medium [2,7]. The reliability of our experimental findings is confirmed by a recent publication of five momentum correlation maps obtained from triple-coincidence measurements of dissociative recombination of H_3 and D_3 with cesium [6]. These maps are in excellent agreement with our data.

Finally, the momentum correlation maps provide extensive and detailed experimental information of one of the most fundamental molecular systems. We hope that this data with its different grades of complexity will trigger efforts from the theorist's side to improve the understanding of this matter step by step.

ACKNOWLEDGMENTS

This research was supported by TP C13 of the Sonderforschungsbereich 276 of the Deutsche Forschungsgemeinschaft.

APPENDIX: DALITZ PLOTS AND HYPERSPHERICAL COORDINATES

In this appendix we first explain how to read momentum correlation maps in Dalitz coordinates, then how to use hyperspherical coordinates and finally how the two are connected with each other. Note that we consider only the special case of three identical nuclei.

The three center-of-mass momentum vectors $\{\vec{k}_1, \vec{k}_2, \vec{k}_3\}$ of the fragments underlie momentum conservation

$$\vec{k}_1 + \vec{k}_2 + \vec{k}_3 = 0.$$

Thus these vectors are arranged in a plane whose orientation in the laboratory frame is described by two angles (θ, ϕ) [44]. The total kinetic energy W of Eq. (3) is determined by the dissociating molecular state. The residual information can be described by three parameters. These can be chosen such that two of them describe the shape of the triangle that is spanned by the vectors \vec{k}_i (what we call the momentum configuration), while the third one gives the orientation of this triangle in the laboratory frame. An elegant way to describe the momentum configuration was introduced by Dalitz [59]. For each event, we plot

$$\epsilon_3 - \frac{1}{3} \text{ vs } \frac{\epsilon_1 - \epsilon_2}{\sqrt{3}},$$

where

$$\epsilon_i = |\vec{k}_i|^2 / (2mW)$$

is the energy normalized single atom translational energy (thus the sum of the three ϵ_i equals unity). For a sufficient amount of data this plot gives the probability-density of the vector correlation. Figure 6 illustrates the connection between specific locations in the Dalitz plot and the associated momentum configurations. Due to momentum conservation, the Dalitz plot is restricted to an area inside a circle with radius $1/3$. The Dalitz plot provides an equal mapping of the phase-space density. It has to be considered that in the case of three indistinguishable particles the Dalitz circle has D_{3h} symmetry with six sectors containing identical information.

It may be useful to specify the locations of the essential configurations in a Dalitz plot. These are characterized in Fig. 6 as follows:

- (a) Center of the plot \leftrightarrow equilateral triangle.
- (b) Dashed straight lines \leftrightarrow acute isosceles triangles.
- (c) Solid straight lines \leftrightarrow obtuse isosceles triangles.
- (d) Outer circle \leftrightarrow linear configurations.

For the description of H_3^+ or H_3 various kinds of internal coordinates have been used. The choice depends on the task and is different, e.g., for the representation of large parts of dissociative surfaces [12] or the calculation of rovibrational levels in a potential well [32]. Hyperspherical coordinates can be used for both requirements. There are no built-in Morse functions as, e.g., in the coordinates proposed by Meyer *et al.* [29] but they are symmetry-adapted and Carter and Meyer [60] have shown how to calculate rovibrational energy levels of triatomic molecules.

Internal coordinates for a three-body system can be distinguished according to the number of length coordinates and angles. Jacobian coordinates consist of two lengths and one angle and are therefore suited for describing a two-fragment dissociation (atom plus diatom) whereas hyperspherical coordinates (two angles, one length, all distances increase uniformly) are appropriate to a three-body breakup. On the other hand Jacobian coordinates are not unique (the same nuclear arrangement can be defined with different coordinates) in contrast to hyperspherical coordinates.

In hyperspherical coordinates ρ , ϑ , φ the sides a , b , c of a triangle are

$$a = 3^{-1/4} \rho [1 + \cos \vartheta \cos(\varphi + 120^\circ)]^{1/2},$$

$$b = 3^{-1/4} \rho [1 + \cos \vartheta \cos(\varphi - 120^\circ)]^{1/2},$$

$$c = 3^{-1/4} \cdot \rho \cdot (1 + \cos \vartheta \cos \varphi)^{1/2}.$$

For a system of three equal masses this definition is the same as the one given by Johnson [61] except for a phase shift of the angle coordinates (cos must be replaced by sin in the above equations). It should also be noted that the coordinates introduced by Dykstra *et al.* [62] (see also [18]) in many aspects resemble the hyperspherical coordinates.

Triangles are characterized by the hyperspherical coordinates in the following way: All triangles with the same values of ϑ and φ are similar (have the same angles); their size is given by $\rho^2 = (a^2 + b^2 + c^2) / \sqrt{3}$. For fixed values of ρ and ϑ all triangles have the same area $0.25\rho^2 \sin \vartheta$, independent of φ . For $\varphi = 0^\circ$ we have acute isosceles triangles, for $\varphi = 60^\circ$ they are obtuse isosceles. Triangles with $\varphi = 30^\circ$ are intermediate between acute and obtuse; the difference of the squares of the long and the middle side is equal to the squares difference of the middle and the short side. $\vartheta = 90^\circ$ means the same equilateral triangle for all values of φ . $\vartheta = 0^\circ$ means linear arrangements; if $\vartheta = 0^\circ$ and $\varphi = 60^\circ$ two nuclei coincide.

For a given value of ρ all possible triangles have values $0^\circ \leq \vartheta \leq 90^\circ$ and $0^\circ \leq \varphi \leq 60^\circ$. In this case a is the shortest, c the longest side of the triangle, and different coordinates correspond to different triangles. The points $\varphi \pm 120^\circ$ are equivalent to $\varphi = 0^\circ$. Because of the properties of trigonometric functions the coordinates $\pm \vartheta$ are equivalent as well as $\pm \varphi$ and in particular the points (ϑ, φ) and $(180^\circ - \vartheta, 60^\circ - \varphi)$. Therefore the set of triangles can alternatively be mapped in a unique way to coordinates $0^\circ \leq \vartheta \leq 180^\circ$ and $0^\circ \leq \varphi \leq 30^\circ$ (but for $\vartheta > 90^\circ$ the ordering of the sides is different). This second mapping has been used (with $\varphi = 0^\circ$) for the Figs. 1–4.

The angles ϑ and φ can be viewed as describing latitudes and longitudes on a sphere of radius ρ , with equilateral triangles at the poles and linear structures on the equator. (This geographical analogy is the reason why we use a different definition for ϑ than other authors.) $\vartheta = 0^\circ$, $\varphi = 0^\circ$, and $\pm 120^\circ$ mean three different orientations of a system in $D_{\infty h}$ symmetry; for the appropriate value of ρ these coordinates correspond to the three saddle points mentioned in Sec. II A. On each hemisphere the complete set of triangles with fixed ρ is mapped six times.

We note for the following that the side bisector s_a in the triangle is given by

$$s_a^2 = -\frac{1}{4}a^2 + \frac{1}{2}b^2 + \frac{1}{2}c^2,$$

etc. In the case of three particle fragmentation the side bisectors of the H_3 triangle can be viewed as the momenta of the fragments in the center of mass system; it is easy to see that their vector sum vanishes. Their squares are then proportional to the kinetic energies of the fragments and the sum of the squares to the total kinetic energy W , but also to ρ^2 (independent of ϑ and φ). For comparison with the ϵ_i of the Dalitz plot the side bisectors must be renormalized such that the sum of their squares equals unity

$$\tilde{s}_a^2 = \frac{1}{3} \left(1 + \frac{1}{2} \cos \vartheta \cos \varphi + \frac{\sqrt{3}}{2} \cos \vartheta \sin \varphi \right) \sim \epsilon_1,$$

$$\tilde{s}_b^2 = \frac{1}{3} \left(1 + \frac{1}{2} \cos \vartheta \cos \varphi - \frac{\sqrt{3}}{2} \cos \vartheta \sin \varphi \right) \sim \epsilon_2,$$

$$z_c^2 = \frac{1}{3} \cdot (1 - \cos \vartheta \cos \varphi) \sim \epsilon_3$$

and it follows that the x and y coordinates of the Dalitz plot can be expressed by the hyperspherical angles ϑ and φ ,

$$x \sim \frac{\epsilon_1 - \epsilon_2}{\sqrt{3}} = \frac{1}{3} \cos \vartheta \sin \varphi,$$

$$y \sim \epsilon_3 - \frac{1}{3} = -\frac{1}{3} \cos \vartheta \cos \varphi.$$

Thus $(1/3)\cos \vartheta$ corresponds to the distance from the center in the Dalitz plot and φ to the polar angle (or the Dalitz plot is the projection of the sphere mentioned above onto the plane containing the equator). In the same way Fig. 6 can also be used to visualize the shape of the triangles defined with hyperspherical coordinates.

-
- [1] A. Suzor-Weiner and I. F. Schneider, *Nature* **412**, 871 (2001).
 [2] V. Kokoouline, C. H. Greene, and B. D. Esry, *Nature* **412**, 891 (2001).
 [3] P. C. Cosby and H. Helm, *Phys. Rev. Lett.* **61**, 298 (1988).
 [4] J. Peterson, P. Devynck, C. Hertzler, and W. Graham, *J. Chem. Phys.* **96**, 8128 (1992).
 [5] U. Müller and P. Cosby, *J. Chem. Phys.* **105**, 3532 (1996).
 [6] C. M. Laperle, J. E. Mann, T. G. Clements, and R. E. Continetti, *Phys. Rev. Lett.* **93**, 153202 (2004).
 [7] D. Strasser, L. Lammich, H. Kreckel, S. Krohn, M. Lange, A. Naaman, D. Schwalm, A. Wolf, and D. Zajfman, *Phys. Rev. A* **66**, 032719 (2002).
 [8] J. Hirschfelder, H. Eyring, and N. Rosen, *J. Chem. Phys.* **4**, 121 (1936).
 [9] R. Porter, R. Stevens, and M. Karplus, *J. Chem. Phys.* **49**, 5163 (1968).
 [10] B. Liu, *J. Chem. Phys.* **58**, 1925 (1973).
 [11] P. Siegbahn and B. Liu, *J. Chem. Phys.* **68**, 2457 (1978).
 [12] D. Truhlar and C. Horowitz, *J. Chem. Phys.* **68**, 2466 (1978).
 [13] A. Varandas, F. Brown, C. Mead, D. Truhlar, and N. Blais, *J. Chem. Phys.* **86**, 6258 (1987).
 [14] S. Mahapatra and H. Köppel, *J. Chem. Phys.* **109**, 1721 (1998).
 [15] R. Bruckmeier, C. Wunderlich, and H. Figger, *Phys. Rev. Lett.* **72**, 2550 (1994).
 [16] R. Azinovic, R. Bruckmeier, C. Wunderlich, H. Figger, G. Theodorakopoulos, and I. D. Petsalakis, *Phys. Rev. A* **58**, 1115 (1998).
 [17] S. Harich, D. Dai, C. Wang, X. Yang, S. Chao, and R. Skodje, *Nature* **419**, 281 (2002).
 [18] C. Nager and M. Jungen, *Chem. Phys.* **70**, 189 (1982).
 [19] H. King and K. Morokuma, *J. Chem. Phys.* **71**, 3213 (1979).
 [20] I. Petsalakis, G. Theodorakopoulos, and J. Wright, *J. Chem. Phys.* **89**, 6850 (1988).
 [21] Z. Peng, S. Kristyan, A. Kuppermann, and J. S. Wright, *Phys. Rev. A* **52**, 1005 (1995).
 [22] I. Mistrík, R. Reichle, U. Müller, H. Helm, M. Jungen, and J. A. Stephens, *Phys. Rev. A* **61**, 033410 (2000).
 [23] I. Schneider and A. Orel, *J. Chem. Phys.* **111**, 5873 (1999).
 [24] V. Kokoouline and C. H. Greene, *Phys. Rev. A* **69**, 032711 (2004).
 [25] M. Jungen, *J. Chem. Phys.* **71**, 3540 (1979).
 [26] K. Kaufmann, M. Jungen, and H.-J. Werner, *J. Chem. Phys.* **87**, 3806 (1983).
 [27] M. Jungen, M. Lehner, and R. Guérout, *Khim. Fiz.* **23**, 71 (2004).
 [28] K. Kaufmann, W. Baumeister, and M. Jungen, *J. Phys. B* **22**, 2223 (1989).
 [29] W. Meyer, P. Botschwina, and P. Burton, *J. Chem. Phys.* **84**, 2891 (1986).
 [30] S. Miller and J. Tennyson, *J. Mol. Spectrosc.* **126**, 183 (1987).
 [31] W. Cencek, J. Rychlewski, R. Jaquet, and W. Kutzelnigg, *J. Chem. Phys.* **108**, 2831 (1998).
 [32] R. Jaquet, W. Cencek, W. Kutzelnigg, and J. Rychlewski, *J. Chem. Phys.* **108**, 2837 (1998).
 [33] L. Schaad and W. Hicks, *J. Chem. Phys.* **61**, 1934 (1974).
 [34] R. Ahlrichs, C. Votava, and C. Zirz, *J. Chem. Phys.* **66**, 2771 (1977).
 [35] R. Mulliken, *Chem. Phys. Lett.* **25**, 305 (1974).
 [36] K. Kulander and M. Guest, *J. Phys. B* **12**, L501 (1979).
 [37] R. Abrol, A. Shaw, A. Kuppermann, and D. Yarkony, *J. Chem. Phys.* **115**, 4640 (2001).
 [38] W. Kolos and L. Wolniewicz, *J. Chem. Phys.* **43**, 2429 (1965).
 [39] I. Dabrowski and G. Herzberg, *Can. J. Phys.* **58**, 1238 (1980).
 [40] N. Bjerre, I. Hazell, and D. Lorents, *Chem. Phys. Lett.* **181**, 301 (1991).
 [41] U. Müller, T. Eckert, M. Braun, and H. Helm, *Phys. Rev. Lett.* **83**, 2718 (1999).
 [42] U. Müller, M. Beckert, and M. Braun, *Rev. Sci. Instrum.* **71**, 4535 (2000).
 [43] M. Beckert and U. Müller, *Eur. Phys. J. D* **12**, 303 (2000).
 [44] U. Galster, P. Kaminski, M. Beckert, H. Helm, and U. Müller, *Eur. Phys. J. D* **17**, 307 (2001).
 [45] G. Gellene and R. Porter, *J. Chem. Phys.* **79**, 479 (1983).
 [46] L. Lembo and H. Helm, *Chem. Phys. Lett.* **163**, 425 (1989).
 [47] L. Lembo, H. Helm, and D. Huestis, *J. Chem. Phys.* **90**, 5299 (1989).
 [48] U. Müller, U. Majer, R. Reichle, and M. Braun, *J. Chem. Phys.* **106**, 7958 (1997).
 [49] U. Müller, M. Braun, R. Reichle, and R. Salzgeber, *J. Chem. Phys.* **108**, 4478 (1998).
 [50] I. Mistrík, R. Reichle, H. Helm, and U. Müller, *Phys. Rev. A* **63**, 042711 (2001).
 [51] G. Herzberg and J. Watson, *Can. J. Phys.* **58**, 1250 (1980).
 [52] G. Herzberg, H. Lew, J. Sloan, and J. Watson, *Can. J. Phys.* **59**, 428 (1981).
 [53] P. Cosby and H. Helm, *Chem. Phys. Lett.* **152**, 71 (1988).
 [54] W. Ketterle, H.-P. Messmer, and H. Walther, *Europhys. Lett.* **8**, 333 (1989).
 [55] G. Herzberg, J. Hougen, and J. Watson, *Can. J. Phys.* **60**, 1261 (1982).
 [56] U. Galster, U. Müller, and H. Helm, *Phys. Rev. Lett.* **92**, 073002 (2004).
 [57] H. Köppel, W. Domcke, and L. S. Cederbaum, *Adv. Chem.*

- Phys. **57**, 59 (1984).
- [58] M. Walter, J. Phys. B **38**, 1845 (2005).
- [59] R. H. Dalitz, Philos. Mag. **44**, 1068 (1953).
- [60] S. Carter and W. Meyer, J. Chem. Phys. **93**, 8902 (1990).
- [61] B. Johnson, J. Chem. Phys. **73**, 5051 (1980).
- [62] C. Dykstra, A. Gaylord, W. Gwinn, W. Swope, and H. Schaefer, J. Chem. Phys. **68**, 3951 (1978).
- [63] An electronic copy of Ref. [27] can be obtained from the author.
- [64] In D_{3h} symmetry the $^2A'_2$ potential correlates with the $4fa'_2$ Rydberg state at equilibrium geometry due to an anticrossing of the latter with a resonance state of the same symmetry near $\rho=4a_0$.
- [65] From emission lines observed by Herzberg *et al.* [55], one can conclude that the data of $H_33pe'(0,0)$ includes a major portion of the $[N=1, G=0, U=1]$ rotational level.
- [66] This additional path is likely the origin for the much more rapid predissociation of $4s$ and $5s$ when compared to $3s$.